Multiconfigurational Approach to X-ray Spectroscopy of Transition Metal Complexes

Marcus Lundberg and Mickaël G. Delcey

Abstract Close correlation between theoretical modeling and experimental spectroscopy allows for identification of the electronic and geometric structure of a system through its spectral fingerprint. This is can be used to verify mechanistic proposals and is a valuable complement to calculations of reaction mechanisms using the total energy as the main criterion. For transition metal systems, X-ray spectroscopy offers a unique probe because the core-excitation energies are element specific, which makes it possible to focus on the catalytic metal. The core hole is atom-centered and sensitive to the local changes in the electronic structure, making it useful for redox active catalysts. The possibility to do time-resolved experiments also allows for rapid detection of metastable intermediates. Reliable fingerprinting requires a theoretical model that is accurate enough to distinguish between different species and multiconfigurational wavefunction approaches have recently been extended to model a number of X-ray processes of transition metal complexes. Compared to ground-state calculations, modeling of X-ray spectra is complicated by the presence of the core hole, which typically leads to multiple open shells and large effects of spin–orbit coupling. This chapter describes how these effects can be accounted for with a multiconfigurational approach and outline the basic principles and performance. It is also shown how a detailed analysis of experimental spectra can be used to extract additional information about the electronic structure.

M. Lundberg (✉) · M. G. Delcey (✉)
Department of Chemistry - Ångström Laboratory, Uppsala University,
751 21 Uppsala, Sweden
e-mail: marcus.lundberg@kemi.uu.se

M. G. Delcey
e-mail: mickael.delcey@kemi.uu.se

E. Broclawik et al. (eds.), *Transition Metals in Coordination Environments*,
Challenges and Advances in Computational Chemistry and Physics 29,
https://doi.org/10.1007/978-3-030-11714-6_7

1 X-ray Spectroscopy for Transition Metals

First-row transition metals are key components of many catalytic systems. Insights into their mechanisms can help in improving their efficiency and stability. Theoretical chemistry is frequently used to predict mechanisms of transition metal-catalyzed reactions. This is typically done by using the relative energy to distinguish between different geometric and electronic structures. To reliably identify a given species requires that the deviations from experiment are smaller than the energy differences between the alternative species. However, this can be very difficult to achieve for systems with several states close in energy, as is often the case for transition metal complexes. Mechanistic predictions also rely on the total charge of the system, which can be difficult to assign a priori. Despite the successful efforts to improve calculations of relative energies, modeling results often require validation by evaluating spectroscopic signatures of key intermediates.

In this chapter, we outline how X-ray spectroscopy, in combination with theoretical modeling, can be used to identify and characterize the electronic structure of transition metal systems. In X-ray spectroscopy, a high-energy photon interacts with the sample and when the photon energy matches the energy required to excite a core electron, the absorption intensity gets an edge-like increase. For first-row transition metals, the most commonly studied core excitations are from the L shell (mainly 2*p*) and are called L-edges, and the K shell (1*s*), called K edges, see Fig. 1 [20]. X-ray spectroscopy has a number of advantageous properties compared to other experimental techniques. The energy required to excite core electrons is element specific, which makes it possible to selectively study the catalytic metal in a complex system. Relevant examples are solar fuel systems that catalyze the formation of chemical fuels from solar energy, with plant photosynthesis being the most well-known system. Here intense transitions in the chromophores designed to maximize light absorption obscure many spectral probes of the catalyst itself [96]. As seen in Fig. 2, the core hole excitation is very localized and X-ray spectroscopy thus selectively probes charge and spin density on the metal [20, 49]. This makes it a widely used tool to extract oxidation and spin state of catalytic metals. X-ray spectra can be obtained

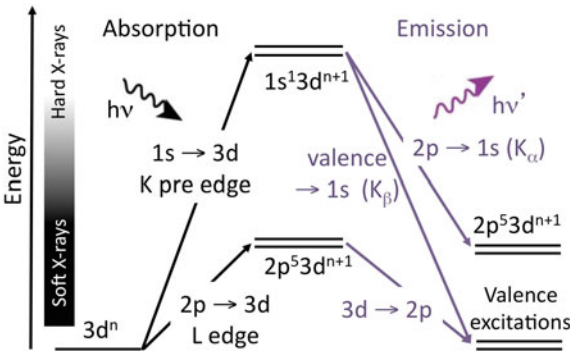

Fig. 1 Selected X-ray processes directly involving the metal 3*d* orbitals in both hard (high-energy) and soft (low-energy) X-ray regions, including X-ray absorption, X-ray emission and resonant inelastic X-ray scattering. Relative energies of different states are not to scale

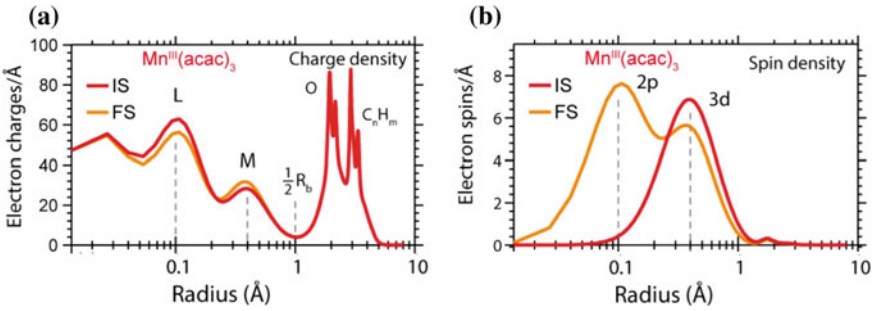

Fig. 2 Radial extension of the $2p$ core hole in manganese. **a** Radial charge densities (RCD) from restricted active-space (RAS) calculations of $Mn^{III}(acac)_3$ in the initial state (IS) and averaged over selected final states (FS). **b** Radial spin densities (RSD) from RAS of $Mn^{III}(acac)_3$ in the initial state and averaged over selected final states. The distance scale is logarithmic to enhance visibility at shorter distances. Reproduced from [49] with permission from the Royal Society of Chemistry

with femtosecond resolution to study transient intermediates in ultrafast chemical reactions [93].

The most direct technique to probe the $3d$ orbitals involved in metal–ligand binding and redox reactivity is through metal L-edge ($2p \rightarrow 3d$ excitations) X-ray absorption spectroscopy (XAS), see Fig. 1. L-edge X-ray photoelectron spectroscopy (XPS), where the $2p$ core electron is excited into the continuum, also gives information about the valence electrons through their interactions with the core hole. Although edge energies are element specific, soft X-ray photons in the metal L-edge energy range (hundreds of eV) also have high probability of photoexciting $1s$ electrons of lighter elements like carbon, nitrogen, and oxygen. This background absorption leads to challenges in extracting the metal signal as well as reduction of the metal site by excess photoelectrons [50, 89]. Metals in enzymes and solution systems are, therefore, often probed using hard X-rays (thousands of eV) in the metal K pre-edge ($1s \rightarrow 3d$ excitations). With the development of new intense X-ray sources, both synchrotron and X-ray free-electron lasers (XFELs), it has also become possible to perform the X-ray equivalent of resonance Raman, often called resonant inelastic X-ray scattering (RIXS). With RIXS, it is possible to reach final states corresponding to both core and valence excitations, see Fig. 1.

These various X-ray spectroscopy techniques allow a wealth of information to be gathered from first-row transition metals. However, the resulting spectra are often complicated to interpret. This is especially true for final states with $2p$ holes, as there are strong interactions between the valence electrons and the core hole, as well as a strong spin–orbit coupling in the $2p$ shell. Theoretical models are, thus, necessary to correlate experimental data and electronic structure. Together with the development of new experimental capabilities, there has been an intense effort to develop theoretical models that include all relevant interactions. This chapter will describe the multiconfigurational wavefunction approach based on the complete active-space (CAS)

paradigm [76]. After a short introduction to different X-ray modeling approaches, we will give a step-by-step explanation of the multiconfigurational approach for transition metal systems. This will be followed by examples of how the combination of theory and experiment can give new insights into transition metal chemistry, in areas ranging from femtosecond spectroscopy to biological cofactors [39, 74]. The current limits of the multiconfigurational approach are systems with two transition metals and the final section describes potential improvements to handle more complex systems.

2 Theoretical Simulations of X-ray Spectra

Modeling X-ray spectroscopy includes the same challenges involved in accurate descriptions of valence states, but the presence of a core hole introduces further complications. Taking the metal L-edge XAS spectra of an open-shell system as an example, the final states are affected by both strong $3d$-$3d$ and $2p$-$3d$ correlation, as well as $2p$ and $3d$ spin–orbit coupling (SOC). This complicates the mapping of electronic structure to spectral shape.

On the other hand, due to the local nature of the core hole, atomic models can provide a very efficient description of many X-ray spectroscopies. A standard modeling approach based on this idea is the charge-transfer multiplet (CTM) method [31, 87]. In this model, initial and final states are calculated from an atomic full configuration interaction (CI) including $2p$ and $3d$ orbitals, i.e., taking into account all possible $3d$ electron configurations. Ligands are described by an empirical ligand-field splitting and to model more covalent interactions, ligand-to-metal charge-transfer (LMCT) or metal-to-ligand charge-transfer (MLCT) configurations can be added in the CI. This method is not only conceptually simple but also computationally inexpensive and has historically been one of the dominant ways to theoretically reproduce X-ray spectra of transition metals and to interpret them in intuitive terms. However, the CTM method includes parameters that are fitted to the experimental spectrum, which makes it less suitable for predictive purposes. Additionally, the number of model parameters increases with decreasing symmetry, and the semiempirical CTM approach thus works best for complexes with a high degree of symmetry.

If the aim is to predict the spectral fingerprint of a molecule and distinguish between different electronic structure alternative, ab initio approaches are preferable as they are independent from semiempirical parameters. A detailed review of ab initio methods for X-ray spectroscopy simulation can be found in [67]; for our purpose here, we will only provide a short overview. Formally, any quantum chemistry method able to describe valence excitations can be extended to the X-ray regime. However, most methods typically generate excited states in energy ordering, so the main change needed in the formalism is a way to target the proper energy range without first having to compute all valence states. Various ideas have been proposed and implemented such as core–valence separation [14, 84], efficient energy-specific eigenvalue solvers [54], and the complex polarization propagator (CPP) [22]. Those formalisms are

general and have been applied to many standard quantum chemistry methods such as density functional theory (DFT) [84], algebraic diagrammatic construction (ADC) [38], and coupled cluster [17]. Yet, as is the case for ground state chemistry and UV–visible spectroscopy, transition metal complexes are particularly challenging, due to their open-shell electronic structures and strong correlation, and some of the methods mentioned above cannot be trusted in this context.

Thanks to its low cost and reasonable accuracy, time-dependent density functional theory (TD-DFT) is widely used. DFT can also be used in conjunction with wavefunction methods such as in the DFT/restricted open-shell CI singles (ROCIS), where a CI with single excitations is built and DFT correlation is added using three system-independent parameters [75]. These DFT-based methods typically fail if the ground states have significant multi-reference character, which is frequent for first-row transition metals. In addition, there is often a strong functional dependence, reducing the predictive power of the method as different functionals can lead to different conclusions. In particular, self-interaction error has a strong effect on the calculated spectrum, the low spatial overlap between core and valence orbitals creating what can effectively be considered to be a charge-transfer excitation, which is an important weakness of some DFT functionals and leads to a critical dependence on the amount of Hartree–Fock exchange [65].

An electronic structure approach that is well suited for transition metal systems is the multiconfigurational (MC) self-consistent field (SCF) method, among which the complete active-space (CASSCF) version is the most widely used [76]. Multiconfigurational methods can be adapted to X-ray processes by including also core electrons in the excitation space [1, 2, 40]. As the number of excitations from the core orbitals can typically be restricted to one, it becomes convenient to use a restricted active space (RAS) wavefunction [62]. This approach has become a leading method to simulate X-ray spectra of smaller transition metal complexes [10, 42, 43, 71, 72]. It can, with minor adaptations, be applied to L-edge XAS and RIXS dominated by electric dipole transitions between bound states [6, 71, 92]. By including second-order terms in the wave vector expansion, electric dipole forbidden transitions in metal K pre-edge XAS and RIXS can be described [32, 33]. With these developments, multiconfigurational methods have now been used to describe all X-ray processes shown in Fig. 1. With recent extensions to continuum excitations, it is also possible to calculate XPS [29, 43]. The combination of an ab initio philosophy with good accuracy provides a powerful predictive tool for the analysis of X-ray spectra. In the following section, we will discuss the basic principles of the multiconfigurational approach, and how to design calculations to get accurate and reliable results.

3 Multiconfigurational Approach to X-ray Processes

The multiconfigurational active-space methods are based on the division of the orbital space into a small set of so-called active orbitals and a larger set of inactive orbitals [79]. Within the active orbitals, electron correlation is treated accurately with CI.

Both CI coefficients and orbital shapes are optimized. Correlation outside of the active space can be treated with a low-level method, typically second-order perturbation theory (PT2). Basic equations for the active-space methods can be found in Chap. 5 of this book. Although multiconfigurational methods are essentially ab initio, their accuracy and computational cost can be tuned through the choice of a number of simulation parameters, with the most critical choice being the choice of orbitals in the active space. This flexibility, together with the relatively high-computational cost, necessitates an understanding of the effect of model choices on the cost and accuracy of the calculation. To demonstrate the methodology and the impact of the different parameters, we will in this section extensively use examples from L-edge XAS modeling of ferric ($3d^5$) reference systems with well-known electronic structures, namely high-spin $[FeCl_6]^{3-}$ (ferric chloride) and low-spin $[Fe(CN)_6]^{3-}$ (ferricyanide) [23, 71, 73].

3.1 System Selection

Before starting the modeling, as with any theoretical chemistry calculation, the first step is the choice of the system. This choice is constrained by the cost of the calculation. The cost of multiconfigurational methods depends on both the total system size and the size of the active space. The active space will be discussed in more details in the next paragraph, but the severe scaling with respect to the number of active orbitals typically restricts calculations to a single transition metal center, as opposed to DFT where large clusters [60], and even extended systems can be described [13]. On the other hand, the scaling with system size is less drastic, especially if PT2 calculations can be avoided. For example, X-ray calculations of the heme iron systems with more than forty heavy atoms have been performed using RAS [34, 74]. Additionally, due to the locality of X-ray spectroscopy, the convergence of the spectrum with the system size is expected to be rapid, allowing more crude models than would otherwise be recommended. Because of the prohibitive cost of geometry optimization with correlated multiconfigurational methods, starting geometries are often taken from experiments or from another level of theory, typically DFT. It is worth noting that in some cases, especially for very covalent metal–ligand bonds with strong multiconfigurational effects, the starting geometry can be of insufficient quality for accurate spectrum calculations. In such cases, reoptimization of a few geometrical parameters can be performed with multiconfigurational perturbation theory [85]. Finally, environment effects can be included in the same way as for calculations of valence states, such as the polarizable continuum model to describe solvent effects [18, 50].

3.2 Active-Space Selection

The second step in the design of the calculation is the choice of the active space, the trademark of multiconfigurational methods. The general rules for any application are to include in the active space any orbital participating in strong correlation. For electronic excitations, any orbital whose occupation is expected to change significantly should also be included. In practice, this selection requires both expertise and experience. Aiming at making multiconfigurational calculations more black box, there have been developments toward automated active-space selection where the selection criteria are meant to optimize the description of strong correlation [83]. However, such criteria cannot be directly applied to spectrum calculations as the orbitals important to describe the photoexcitation process are not necessarily the same that contribute most to correlation. In practice, the final choice of active space is still driven by chemical intuition and experience.

For transition metals, there is a wealth of experience on the choice of active space to describe strong correlation and intuitive rules have been compiled [69]. For X-ray spectroscopy, where the range of final states span over several eV, the target accuracy is typically lower than most other applications and the active space can be reduced somewhat. One can often satisfactorily restrict the selection to the metal 3*d* orbitals and any ligand orbitals forming strong covalent bonds with the metal. Local symmetry, either strict or approximate, can significantly help reducing the number of ligand orbitals included. To this space, one should add orbitals that are excited to or from in the X-ray process, which typically are virtual orbitals with some metal content and the core orbitals. When using the RAS formalism, the core orbitals are conveniently put in the ras1 space allowing a single excitation as most processes include a single core hole. The orbitals involved in metal–ligand bonding are typically put in ras2 to allow all possible configurations, see Fig. 3a.

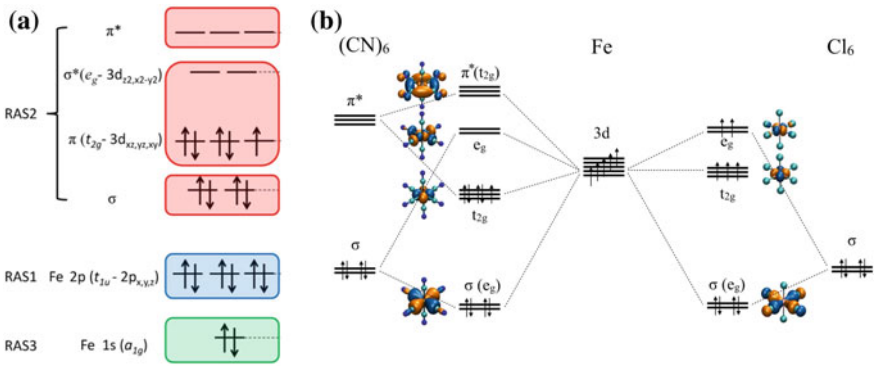

Fig. 3 **a** Active space for RAS calculation of 1*s*2*p* RIXS of iron hexacyanides. Reproduced from [32] with permission from the American Chemical Society. **b** Schematic orbital diagram of $[Fe(CN)_6]^{3-}$ and $[FeCl_6]^{3-}$. Only selected ligand orbitals are shown

The orbital diagrams of ferricyanide and ferric chloride are shown in Fig. 3b. An active space for valence calculations of $FeCl_6$ would include the five $3d$ orbitals and the two e_g ligand orbitals combinations forming the σ bond with the metal. For accurate energy calculations, it is recommended to include an additional set of metal d-type orbitals, the double shell, for a total of twelve active orbitals [69]. However, for X-ray calculations, neglecting the double shell gives small differences in the spectrum [71]. As the complex is relatively ionic, the ligand-dominated σ orbitals have limited metal d character, and one could imagine limiting the active space to the five $3d$ orbitals. Yet, with this choice of orbitals, the subsequent second-order perturbation theory calculation fails to converge (see Sect. 3.5), a typical sign of an ill-balanced active space. This example thus shows that the final choice of active space is usually a dialogue between the user and the program.

For $Fe(CN)_6$, the situation is similar except that this time, the ligands have empty π^* orbitals able to form a bond with the metal t_{2g} orbitals through π-backdonation. This stabilizes the t_{2g} orbitals and thus increases the gap with the e_g, which favors the low-spin configuration. As the π^* orbitals are empty and have some $3d$ character, they can be populated by X-ray absorption and are needed in the active space, consisting thus of ten orbitals.

In some cases, the X-ray process involves two different core levels. One example is $1s2p$ RIXS, where $1s \rightarrow 3d$ absorption is followed by monitoring the strongest emission channel, $2p \rightarrow 1s$, see Fig. 1. Modeling of this process requires independent control of the core-hole occupations. In a RAS calculation, this can be achieved by placing the two sets of core orbitals in different ras spaces, typically $2p$ in ras1 and $1s$ in ras3 and thus, both $1s$ and $2p$ core-hole states can be computed with the same active space, see Fig. 3a [32].

3.3 Generating Core-Hole States

To obtain a spectrum, a large number of excited states needs to be computed. As mentioned in the previous section, the target is to generate specific core-excited states, without computing all possible valence states. In some cases, such as L-edge spectra of centrosymmetric complexes, the $2p$ core-hole states can be in different symmetries (ungerade) than the valence states (gerade) and the separation is trivial. For the general case, a simple technique is to remove from the configuration interaction all configurations with fully occupied core orbitals, the so-called core–valence separation (CVS) [14]. For active-space methods, the CVS is closely related to the generalized active-space method [33, 59].

Orbital optimization is typically done using state-average orbitals. This avoids the separate optimization of every state, while ensuring a balanced description of all the states. The main drawback is that the results depend strongly on the number of states, which needs to be taken into account, in particular when comparing calculations with different number of states. During orbital optimization, the algorithm may lower the state average energy by replacing the core orbital by an occupied orbital of higher

energy, for example 3p instead of $2p$. Unless this is prevented using e.g., a restricted step algorithm [40], the core orbitals have to be frozen during the orbital optimization. A downside to this is that this prevents the expected contraction of those orbitals upon core excitation, but the main effect is expected to be a global shift of the final states to higher energy. Often the relative edge position is more important than the absolute one, and the frozen-core approximation has been used to predict oxidation state shifts with errors of 0.3 eV when using the same active space and number of states [33, 49].

3.4 Simulating Light-Matter Interaction

The last step to obtain a spectrum is to compute transition intensities at different wavelengths. For bound states, the intensity can be calculated from the matrix element of the operator representing the light-matter interaction between the initial and final states. Most often, the plane wave representing the light is approximated by an electric dipole. If core-hole states have been optimized separately from the valence states, transition intensities can still be calculated correctly by taking advantage of a biorthogonalization scheme [61]. From the computed intensities, the final spectrum is generated using a Lorentzian lifetime broadening convoluted with a Gaussian broadening to account for the experimental resolution. If only absorption intensities are considered, this corresponds to a spectrum collected in transmission mode. However, the transmission spectra and those obtained by measuring the photoelectron current, the total electron yield, are similar. RIXS spectra can be calculated from the transition intensities for both absorption and emission processes according to the Kramers–Heisenberg formula [25]. L-edge XAS spectra of metal complexes in solution are in many cases collected by measuring the fluorescence from the core-excited states, the partial fluorescence yield (PFY) mode. The PFY-XAS spectra can be calculated from the RIXS cross sections by integrating the relevant emission channels for each incident energy [27, 28, 47].

Results obtained for L-edge XAS of ferric chloride and ferricyanide are shown in Fig. 4 [36, 73, 91]. The spectra are divided into two separate regions, L_3 and L_2, split by the $2p$ spin–orbit coupling, as will be discussed in detail below. RAS calculations can be used to correlate spectra and electronic structure. In ferric chloride, the ligand field is weak and different configurations mix strongly, making it difficult to assign transitions to specific $3d$ orbitals. One exception is the high-energy peak in the L_3 edge that has been identified as a $2p \rightarrow 3d$ transition, combined with a $\sigma \rightarrow 3d$ LMCT [71, 91]. In ferricyanide the ligand field is strong, and a molecular orbital picture becomes more relevant. The sharp first peak corresponds to a $2p$ electron filling the t_{2g} hole and the second peak is an excitation to e_g. The third peak is a signature of π-backbonding and is typically labeled after the π^* molecular orbital, see Fig. 3, but is in reality a strong mix of e_g and π^* contributions [36, 71].

The 1s $\rightarrow$ 3d transitions of K pre-edge are dipole forbidden in centrosymmetric complexes and still relatively weak in many other systems. In the former case,

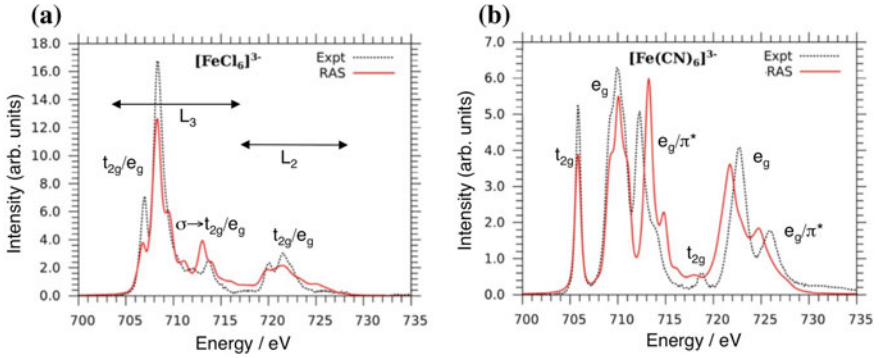

Fig. 4 Comparison between theory and experiment for the iron L-edge X-ray absorption spectra of **a** $[FeCl_6]^{3-}$ and **b** $[Fe(CN)_6]^{3-}$. Adapted from [73] with permission from Wiley

they only gain intensity from what is typically referred to as electric quadrupole transitions. To model these transitions requires a second-order expansion of the electromagnetic wavevector [8], or use of the exact form [55, 56]. Both alternatives have also been used to calculate iron K pre-edges using RAS wavefunctions [33, 81, 82].

While multiconfigurational methods are most often used to describe excitations to bound states, they can also be extended to describe ejection of electrons into the continuum, such as for photoelectron spectroscopy. XPS provides a wealth of information on the electronic structure and can for example be used to study specific solute–solvent interactions of metal complexes in solutions [88]. From a modeling perspective, the key is often to compute the Dyson orbitals, which corresponds to the overlap between the initial N-electron wavefunction and the final $N-1$-electron wavefunction of the ionized molecule. To compute the intensities, one common method is the so-called sudden approximation (SA) that neglects the dependency on the kinetic energy of the outgoing photon and simply estimates the intensity as the norm of the Dyson orbital. However, this approximation is not valid for low-energy photoelectrons, and instead, a more sophisticated approach is to explicitly model the free electron and compute the transition intensity with the Dyson orbital with the help of numerical integration. An efficient implementation of the Dyson orbitals using a biorthonormal basis has recently been implemented in the CAS/RAS framework [29, 30].

XPS spectra for $[Fe(H_2O)_6]^{2+}$ have been calculated using a minimal active space including only the 3*d* orbitals in the valence as shown in Fig. 5a. There is good agreement between RAS modeling and experiment, with much improved results for the full formalism over the sudden approximation, see Fig. 5b. The Dyson orbitals can additionally be analyzed to understand the relation between the experimental features and the electronic structure, see Fig. 5c.

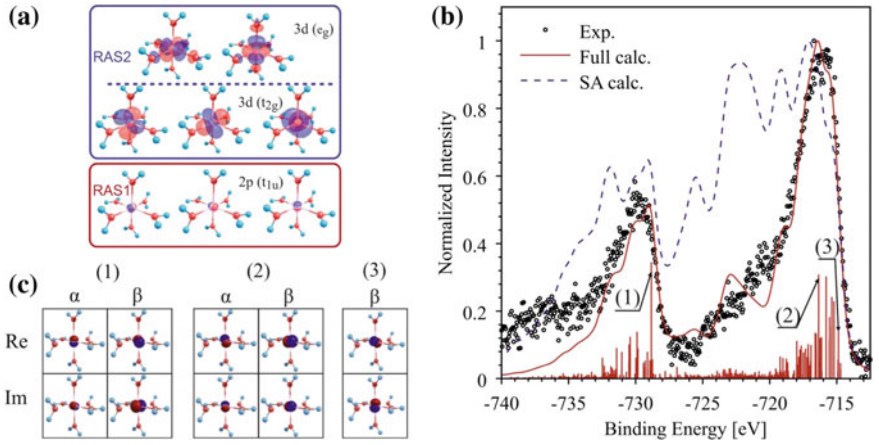

Fig. 5 **a** Orbitals in the active space of $[Fe(H_2O)_6]^{2+}$. **b** Experimental (2M $FeCl_2$ aqueous solution) and calculated ($[Fe(H_2O)_6]^{2+}$ cluster) XPS for incoming photon energy of 925 eV. Full calculation corresponds to numerical integration of XPS matrix element, SA means sudden approximation. **c** Real and imaginary parts of α and β spin contributions to the Dyson orbitals for selected transitions. Adapted from [29], with the permission of AIP Publishing

3.5 *Number of States, Correlation Level and Basis Set*

The simulated spectra shown in Fig. 4 are sensitive to several different modeling parameters, among them the number of states, the level of electron correlation, and the choice of basis set. Even if the computation of all valence states can be avoided, as discussed above, the number of excited states needed to describe an X-ray spectrum can be very large. In transition metal complexes, the density of states tends to be very high, and an X-ray absorption spectrum typically spans 10 eV or more, and often several hundred states are required. As an example, the ferricyanide spectrum displays a strong peak that is associated with the ligand-dominated π^* orbitals, see Fig. 3. However, the goal of the orbital optimization is to minimize the energy, not to reproduce an X-ray spectrum. Unless enough states are included to excite to these orbitals, the optimization prefers to include 4*d*-type orbitals that correlate well with the t_{2g} 3*d* (double-shell effect), but are not particularly relevant to the spectrum. As shown in Fig. 6, at least 320 states were needed to reach the π-backbonding orbitals and reproduce the corresponding peak in the spectrum. Even more states were required to fully converge the spectrum [73]. The large number of states constitutes one of the major limitations of the method, as the cost of the calculation increases at least linearly with this parameter. Additionally, it is difficult to estimate in advance how many states are required. A simple convergence test is to increase the number until the spectrum features remain approximately fixed.

While calculations at the multiconfigurational self-consistent field level often give qualitatively correct descriptions, higher numerical accuracy can be reached

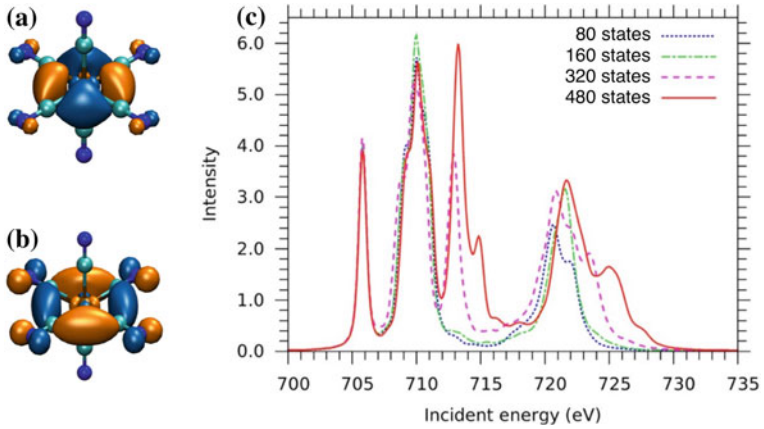

Fig. 6 Effects of number of states on RAS modeling. **a** High-lying t_{2g} orbitals of $4d$ character included with fewer than 80 states. **b** π^* orbital included in the active space with 80 states or more. **c** L-edge XAS spectra of $[Fe(CN)_6]^{3-}$ calculated using RASPT2/ANO-RCC-VTZP with different number of states per spin multiplicity. Adapted from [73] with permission from Wiley

by including dynamical correlation through second-order perturbation theory, either using the second-order complete active-space perturbation theory (CASPT2) [3], its counterpart for a restricted active space (RASPT2) [64], or the N-electron valence perturbation theory (NEVPT2) [4]. The latter two have both been used for calculations of X-ray spectra [16, 42, 73].

The effect of adding a perturbation correction can be seen in Fig. 7. For ferric chloride, focusing on the L_3 edge, the spectrum remains relatively similar, and only the minor $\sigma \rightarrow 3d$ LMCT peak sees a significant shift in position. On the other hand, the effect on ferricyanide is more significant. The t_{2g}-e_g splitting decreases by 1 eV, giving almost perfect agreement with experiment, while the overestimation of the position of the π^* peak drops from 4 to 1 eV. The large effect of the perturbative step

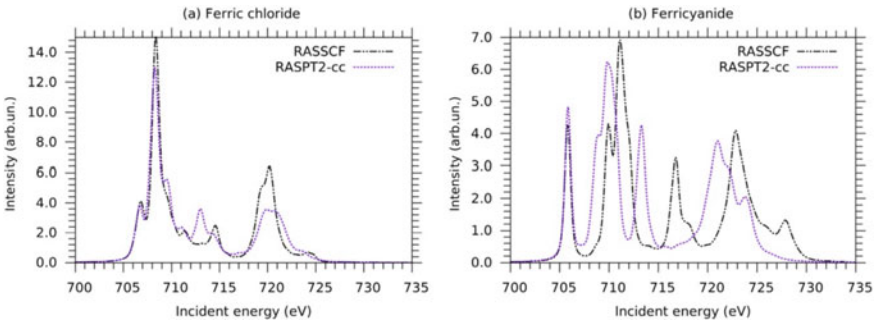

Fig. 7 L-edge XAS spectra of **a** $[FeCl_6]^{3-}$ and **b** $[Fe(CN)_6]^{3-}$ calculated at the RASSCF and RASPT2 levels. Reproduced from [73] with permission from Wiley

on the π backbonding peak actually indicates a missing orbital in the active space, specifically the ligand π which strongly correlates with the π^*. In ferrocyanide ($[Fe(CN)_6]^{4-}$), the error for the corresponding π^* peak drops from 2.0 to 0.6 eV with PT2, while the error in the relative energy of different states in the e_g peak decrease from 0.6 to 0.1 eV [32].

A well-known problem with CASPT2/RASPT2 is the presence of possible intruder states. To reduce this problem, an imaginary shift of 0.3–0.5 hartree can be applied [24]. It is still important to check that the reference weights, i.e., the weight of the RASSCF state in the total correlated wavefunction, are consistent for all core-hole states. Despite being a perturbative approach, the RASPT2 equations are solved iteratively and low reference weights often translate into convergence difficulties and/or inaccurate results. Low weights despite a small imaginary shift most commonly stem from improper active-space selection.

The formulation of CASPT2/RASPT2 also includes one empirical parameter called the ionization potential electron affinity (IPEA) shift, which was introduced to fix a systematic error when dealing with open-shell configurations [26]. There is no consensus on the optimal value of this shift and recent studies suggest that it strongly depends on system, active space and basis set [97]. The IPEA should not be used as an empirical parameter to improve the match with the experimental spectrum, and a large effect of changing the IPEA value indicates that the active space may be too limited, as can be seen for the previously discussed π^* peak in ferricyanide [73]. NEVPT2 does not include any such shift in its formulation and is also less sensitive to intruder states. However, the correlation contribution to the spin-state energetics of some transition metal complexes showed larger deviations for NEVPT2 compared to CASPT2 [70].

Second-order perturbation theory is a correlated method, and thus in theory displays a slow basis set convergence. However, for X-ray calculations no major changes in the spectrum have been observed going beyond a triple-zeta basis set, and in many cases good results are obtained already at the double-zeta level [73]. On the other hand, standard contracted basis sets do not provide much flexibility for core electrons to contract upon excitation or for core correlation. This leads to errors in absolute edge positions of around 3–4 eV for L-edges and up to 18–20 eV for K edges when using a triple-zeta basis set, slightly depending on the active space and the number of states [33, 49, 73]. The errors in the absolute L-edge position can be improved to 0.75 eV with the use of an uncontracted basis set [16], but this is very expensive and only applicable to small systems. In the frozen-core approximation, the quality of the core basis set is less important. However, relative energies between complexes with similar ligand environments and active-space selections can still be reproduced within 0.3 eV [33, 49].

When it comes to spectral shape, RASPT2 calculations typically predict all major peaks in the L_3 edge with at most 30% error in intensity. The largest error in relative energy, around 1 eV, is seen for cases with incomplete active spaces, as in the ferricyanide L-edge XAS π^* peak. That energetic error might seem large, but should

be compared to the 30 eV range of the full spectrum. The accuracy gives, in most cases, sufficient predictive power to identify the charge, spin, or electronic structure of a chemical species [34].

3.6 *Relativistic Effects*

Even for first-row transition metals, because of the direct involvement of core orbitals, relativistic effects are very significant. Scalar relativistic effects affect the energy and radial extent of the core orbitals and thus have a significant effect of the spectrum, though mostly as a global shift. In our methodology, scalar effects are included using a second-order Douglas–Kroll–Hess (DKH) Hamiltonian [21, 35], coupled with a basis set designed specifically to be used in conjunction with DKH, namely the ANO-RCC basis [77, 78].

When dealing with $2p$ core holes, the description of spin–orbit coupling is also essential because the $2p$ orbitals split into 2 spin–orbit levels, $P_{1/2}$ and $P_{3/2}$ separated by around 10 eV (depending on the metal). A computationally efficient way to include spin–orbit coupling in active-space calculations is to compute core-hole states with spin multiplicities $S = 0, \pm 1$ relative to the ground state, and diagonalizing an approximate spin–orbit hamiltonian in the basis of those states [63]. This is equivalent to using Russell-Saunders (LS) coupling. It is only an approximation of the correct four-component solution, but it is significantly simpler and sufficiently accurate for most purposes. A full four-component multiconfigurational code has been applied to X-ray spectroscopy, but only to systems with a small number of active orbitals and without dynamical correlation [7].

The L-edge spectrum from a model low-spin d^5 system in O_h symmetry offers a clear and extensive demonstration of the effect of spin–orbit coupling, see Fig. 8a.

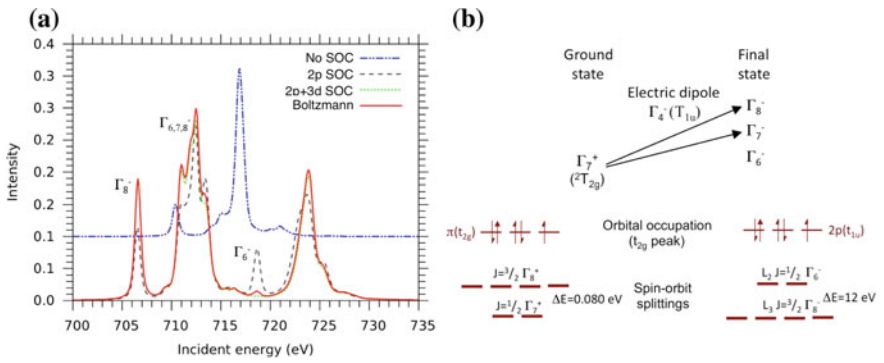

Fig. 8 **a** RAS L-edge XAS spectra of the Fe^{3+} ion with different treatments of $2p$ and $3d$ SOC. Boltzmann referes to a Boltzmann distribution of different SOC ground states. **b** Selection rules for electric dipole transitions using Bethe notation for double groups. Adapted from [71] with the permission of AIP Publishing

As expected, without any SOC, there is a single edge. Inclusion of $2p$ SOC not only splits the spectrum into L_3 ($J_{2p} = \frac{3}{2}$) and L_2 ($J_{2p} = \frac{1}{2}$) edges but also leads to major changes in spectral shape because of the mixing of states with different multiplicity. This shows that the spin–orbit effect cannot always be modeled by simply duplicating the spin-free spectrum and shifting the two edges away from each other. It is also important to note that to form the correct spin–orbit states requires all three $2p$ orbitals in the active space.

The $3d$ SOC constant is much weaker, 0.05 eV for iron, than the $2p$ one (8 eV). However, taking $3d$ SOC into account leads to visible changes in the calculated spectrum, especially in the intensities of the two $2p \rightarrow t_{2g}$ peaks, see Fig. 8. This can be explained by the selection rules, see Fig. 8b. Ignoring Jahn–Teller distortions, which have only minor effects on the energy levels [71], there is triple orbital degeneracy in the ground state. This degeneracy is lifted by spin–orbit coupling, and the lowest spin–orbit states have different selection rules compared to the low-lying excited states and thus generate different spectra.

3.7 Simulating X-ray Processes with Molcas

The X-ray calculations described in this chapter have almost exclusively been performed using the Molcas program [5], which is a leading program for multiconfigurational quantum chemistry. The same capabilities are also available in the open-source distribution OpenMolcas. To facilitate future calculations, Fig. 9 shows the different steps of a RAS X-ray calculation in OpenMolcas. The program is composed of several modules, each performing a specific task with their own input and communicating together through files.

The active space is defined in the input to the `RASSCF` program. As shown in Fig. 3, it is common to place core orbitals in ras1 allowing for at most one excitation. To avoid calculating a large number of valence excited states with filled core orbitals, core–valence separation can be invoked using the *hexs* keyword. To avoid that the

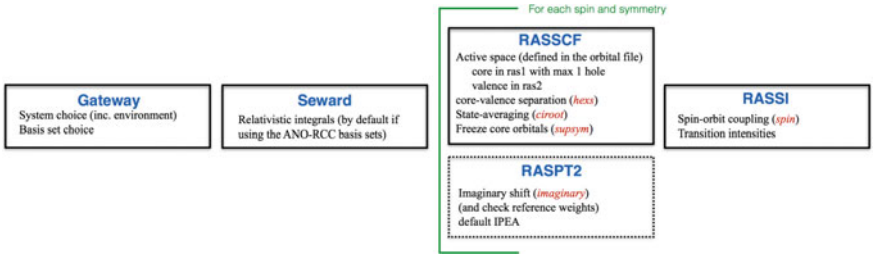

Fig. 9 Calculation template for X-ray simulations with the RAS method in OpenMolcas. The name of the boxes are the names of the OpenMolcas module corresponding to the specific parameters. The red italic text indicates specific keywords

hole rotates out of the target core orbitals, these can be frozen during the orbital optimization using *supsym*. In the RASPT2 program, both imaginary and IPEA shifts can be specified, with default values being 0.1 and 0.25 eV, respectively. Spin–orbit coupled states are formed in a RAS state interaction (SI) algorithm using the *spin* keyword in the RASSI program. RASSI also calculates transition matrix elements between all computed states. The default is the electric dipole approximation but a complete second-order expansion as well as the exact form of the wavevector are also implemented [81, 82]. With most practical aspects of the modeling covered, the next sections will describe applications of X-ray spectroscopy in different fields of chemistry.

4 Electronic Structure from X-ray Spectra

In this section, we will describe how the combination of X-ray experiments and multiconfigurational modeling can be used to extract very detailed information about electronic structure. The first examples show how modeling can be used to characterize the total spin and oxidation state of a complex. The next examples focus on the structure of individual orbitals involved in metal–ligand binding, often through studies of charge-transfer and ligand-field transitions. The examples include both ground-state electronic structures and time-resolved studies of transient reaction intermediates at the femtosecond timescale. The final examples describe the electronic structure at even finer detail by looking into splittings between states with the same formal orbital occupation, in the X-ray field usually called multiplet splittings. These examples illustrate how multiconfigurational methods give a correct description of these different states, and that this can be used to extract detailed orbital information.

4.1 Spin and Oxidation State

Reaction mechanisms of redox reactions can at the most basic level be described in terms of changes of the spin and oxidation states of the metal. X-ray spectroscopy is ideal to observe these effects because the core hole is a very local probe of the metal site as shown in Fig. 2. Multiconfigurational calculations accurately predict oxidation state dependent spectral changes, as has been shown for ferrous ($3d^6$) and ferric ($3d^5$) complexes [10, 32], as well as a series of photocatalytically relevant Mn systems [11]. The predictive power of the simulations makes it possible to identify problems in the experimental data, which is important as many samples easily photodamage in intense X-ray beams [50].

In addition to fingerprinting reaction intermediates, calculations can also be used to understand how oxidation state is reflected in the L-edge XAS spectrum because both redox and core-excitation processes can be treated at an equal level. One of the

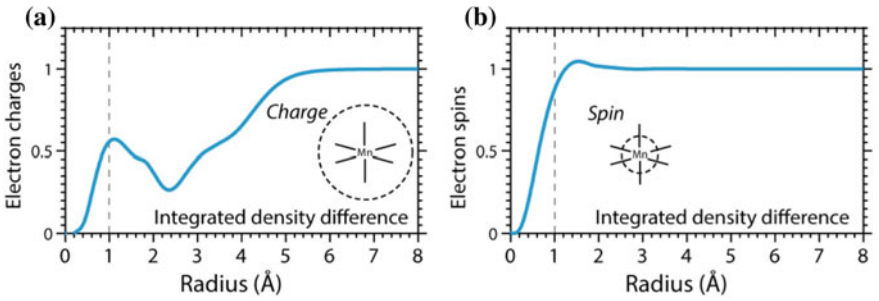

Fig. 10 Changes in spin and charge density upon reduction of $Mn^{III}(acac)_3$. **a** Integrated radial charge density (RCD) difference (RCD of $[Mn^{II}(acac)_3]^{1-}$ minus RCD of $Mn^{III}(acac)_3$. **b** Integrated radial spin density (RSD) difference (RSD of $[Mn^{II}(acac)_3]^{1-}$ minus RSD of $Mn^{III}(acac)_3$. The dashed vertical lines indicate half the Mn-O bond length R_b. Adapted from [49] with permission from the Royal Society of Chemistry

main signatures of increasing metal oxidation state in L-edge spectroscopy is a shift of the absorption edge to higher energy, together with significant changes in spectral shape [19]. These changes can be used to identify species in ultrafast reactions, even for systems as complex as the four-manganese oxygen-evolving complex in photosystem II [46]. Oxidation state should also be possible to identify from the total absorption cross sections, which should be roughly proportional to the number of holes in the 3*d* orbitals [47, 48].

The clear effects of formal oxidation state on X-ray spectra are somewhat intriguing because quantum chemistry calculations show that the charge density of the transition metal does not strongly correlate with its formal oxidation state. Instead the spin density provides a more reliable signature [9, 41]. This can be illustrated for the reduction of the well-known model complex $Mn^{III}(acac)_3$ [49]. Figure 10 shows the calculated changes in charge and spin density upon addition of an electron, while keeping the geometry constant. Charge density is delocalized over the whole molecule due to Coulomb repulsion, even for this relatively ionic complex. In contrast, changes in spin density are localized to the metal atom due to favorable exchange interactions.

In reality, reduction of $Mn^{III}(acac)_3$ leads to geometry changes from octahedral to tetrahedral coordination $Mn^{II}(acac)_2$. The experimental and RAS calculated PFY-XAS spectra of $Mn^{II}(acac)_2$ and $Mn^{III}(acac)_3$ are shown in Fig. 11a, b. The overall agreement is good, with the exception of the position and intensity of the L_2 edge, partially due to problems to describe fluorescence in this edge. Experimentally, the maximum of the L_3 edge is shifted to higher energies by 2.0 eV upon oxidation and the simulations reproduce this shift with only a minor error of 0.3 eV.

Interestingly, the spectral shape can be partially explained by looking at the position of the different spin-state contributions, see Fig. 11c, d. As a result, one can expect that the spectral shape is strongly affected by exchange interactions. As the spin density is strongly localized on the metal, the spectral shape remains atomic

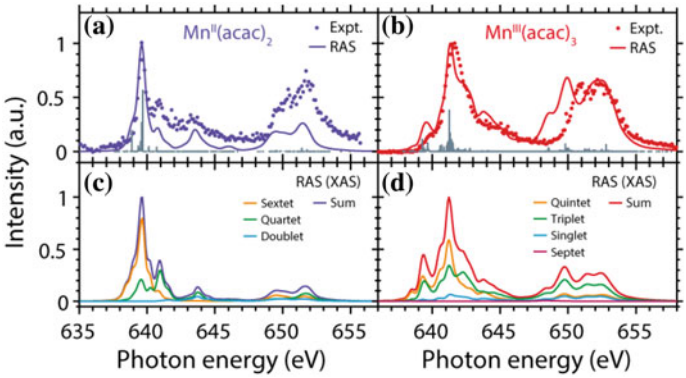

Fig. 11 Experimental and RAS modeling of Mn(acac) complexes. **a**, **b** Calculated RAS and experimental PFY-XAS spectra of **a** $Mn^{II}(acac)_2$ and **b** $Mn^{III}(acac)_3$. **c**, **d** Calculated absorption spectra (XAS not PFY) decomposed into the relative contributions of the (spin) multiplicities in the final states for **c** $Mn^{II}(acac)_2$ and **d** $Mn^{III}(acac)_3$. Reproduced from [49] with permission from the Royal Society of Chemistry

like and provides a signature for the number of spins on the metal. However, the nature of the shift requires a more in-depth analysis, and it was shown that it is due to changes in Coulomb interactions, which depend on the charge density. By studying the charge density changes during core excitation, it is proposed that the core excitation increases the electron affinity in the final state, which leads to lower excitation energies for Mn(II) compared to Mn(III) [49].

The results show that multiconfigurational calculations are able to reproduce spectral changes due to changes in oxidation state, which is important for reliable fingerprinting of reaction intermediates. At the same time, the simulations give additional insights into the molecular origin of these changes and how they are linked to charge and spin density.

4.2 Molecular Orbitals in Metal–Ligand Binding

X-ray spectroscopy does not only give information about spin and oxidation states but also provides detailed information about metal–ligand interactions. This sensitivity has been used to extract ground-state electronic structure by fitting parameters in the parameterized CTM model to the spectrum [36, 91]. For nonparameterized methods like RAS, calculating spectra does not give any new information compared to accurate ground-state calculations. Instead, RAS offers the possibility to rationalize how different spectral features are connected to the electronic structure. However, the strong interactions with the 2*p* hole in the final states lead to complicated electronic structures that, although they can be correctly described in a multiconfigurational model, are difficult to interpret.

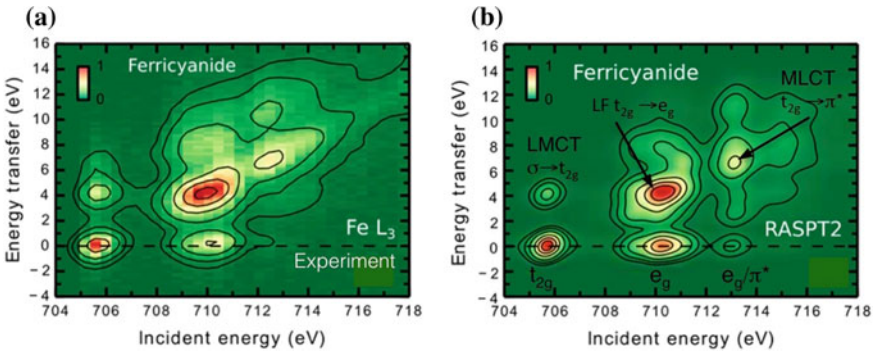

Fig. 12 RIXS maps of ferricyanide at the Fe L_3 edge from **a** experiment and **b** RAS simulations. Adapted from [53] with permission from the American Chemical Society

To get direct access to valence states, it is possible to use L-edge RIXS, see Fig. 1. This is a two-photon process, where absorption of an incident photon (hν) leads to emission of a scattered photon of a different wavelength (hν'). By varying the energy difference between incident and emitted photons, i.e., the energy transfer, different valence states can be accessed. The two-dimensional RIXS spectra provide more information than the one-dimensional XAS spectra and have been used to identify reaction intermediates in ultrafast chemical reactions [39, 51, 52, 66, 90, 93]. To aid in fingerprinting, theoretical models can be used to assign spectral features and extract electronic structure information. The first RIXS applications of RAS targeted ligand-field excitations of metal ions in water [6, 42, 92]. Later studies have focused on highly covalent complexes like $Fe(CO)_5$ and $Fe(CN)_6$ [23, 53, 86, 93]. In this and the following subsection, we will show how RIXS modeling can be used to study molecular orbital interactions in both ground and short-lived excited states of iron hexacyanides.

Ground-state L-edge RIXS spectra have been analyzed for both ferro- and ferricyanide [23, 53], but here only results for the ferric complex will be discussed. Experimental and RAS simulated L-edge RIXS spectra of ferricyanide are shown in Fig. 12. In the two-dimensional spectra, the incident energy axis is the same as in the L-edge absorption. Although the RIXS spectra have been collected over the full incident energy range, only the L_3 edge is shown to better highlight spectral features. As in the L-edge XAS, the resonances along the incident energy axis can be conveniently labeled t_{2g}, e_g, and π^*.

The additional information in the RIXS experiment comes from the energy transfer axis, which corresponds to the valence excitation energies. Starting with the t_{2g} resonance, the peak at 0 eV corresponds to elastic transitions where an electron from the newly closed t_{2g} shell fills the $2p$ hole. The second peak at 4 eV corresponds to emission from a filled orbital. With the help of RAS calculations, this orbital was identified as the ligand-dominated σ orbital shown in Fig. 3. The resonance can thus be assigned as a $\sigma \rightarrow t_{2g}$ LMCT transition.

Proceeding along the incident energy direction, the next resonance is the e_g peak, for which several features along the energy transfer axis can be resolved. After the elastic peak, there is a broad and intense resonance around 4 eV that corresponds to $t_{2g} \rightarrow e_g$ transitions, see Fig. 12. These ligand-field transitions are the most intense in the RIXS spectrum, in contrast to the weak transitions in UV/Vis absorption spectroscopy. This is due to the differences in selection rules. The single-photon $g \rightarrow g$ transition is parity forbidden and only gain intensity through vibronic coupling, while the two-photon $g \rightarrow u \rightarrow g$ transition is parity allowed. In addition, the strong spin–orbit coupling in the intermediate state breaks the spin selection rules, and calculations indicate that both transitions to singlet and triplet final states have appreciable magnitude [53].

Notice that although the $\sigma \rightarrow t_{2g}$ and $t_{2g} \rightarrow e_g$ transitions have similar final-state energies, these resonances are clearly separated along the incident energy in the RIXS map. RIXS thus includes more information than a single-photon absorption, partly due to the enhancement of ligand-field transitions, but also facilitates the assignment of these resonances to different molecular orbital transitions. With the help of electronic structure calculations, the RIXS plane can be used to map out the entire set of valence orbitals.

4.3 Transient Intermediates from Charge-Transfer Excitations

Full understanding of catalytic reactions requires knowledge of intermediates along the reaction pathway. The development of intense XFELs with time resolution in the femtosecond range has opened up new ways to study short-lived intermediates. A prominent example is how the combination of femtosecond RIXS with RAS modeling has given detailed insight into the spin and ligand-exchange dynamics of photoexcited $Fe(CO)_5$ [51, 52, 93]. In general, valence excited states of iron complexes have attracted considerable scientific interest, as charge separation in these states can be used in light-harvesting applications [57]. Again, iron hexacyanide serves as a suitable model system to understand how information about electronic, spin and structural dynamics can be extracted from the combination of modeling and experiment [39, 66].

In the experiment, ferricyanide absorbs a photon from the UV/Vis probe, which leads to an LMCT excitation that fills the t_{2g} shell and at the same time creates a hole on the ligand. The time evolution of this excited state is then followed using femtosecond RIXS [39]. Figure 13a shows the difference spectrum of the LMCT state compared to the ground state of ferricyanide (shown in Fig. 12a). A clear fingerprint of the LMCT state is the complete loss of the t_{2g} peak in the RIXS spectrum, because the hole in that orbital is filled in the valence excitation.

RAS calculations have been used to predict spectra of potential species along the reaction pathway and offer fingerprints for the dynamics [66]. They can also explain

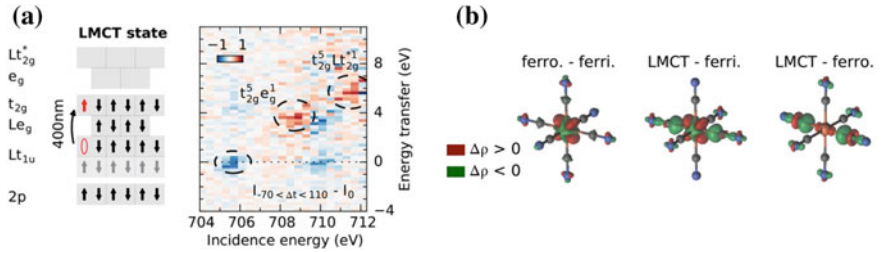

Fig. 13 **a** Valence electronic occupation of the LMCT state and difference map in the range of 70–110 fs. **b** Charge density differences (CDDs) of the LMCT state and ferrocyanide taken with respect to ferricyanide. To isolate ligand-hole effects, the CDD of the LMCT state with respect to ferrocyanide is additionally shown. All differences are calculated at the CASPT2 level at the optimized ferricyanide geometry. Adapted from [39] with permission from the American Chemical Society

how changes in the RIXS spectrum relates to changes in metal–ligand interactions of the ferrocyanide LMCT state compared to the ground states of ferro- and ferricyanide. Although the electronic structure of the excited state can be directly obtained from calculations, the comparison to experiment can verify the predicted changes in metal–ligand interactions. RAS calculations of the charge density difference between the LMCT state and the ferrocyanide ground state, which both have the same nominal $t_{2g}^6 e_g^0$ configuration, show an increase in charge density on the iron along the metal–ligand bond axis, see Fig. 13b. This indicates a net increase in σ-donation in the LMCT state. At the same time, π-backdonation remains largely constant, which gives overall stronger metal–ligand binding in the LMCT state compared to ferrocyanide and a reduced Fe-C bond length [66]. The predicted changes in electronic structure are consistent with a shift in the onset of the edge to lower energies, as well as an increase in the ligand-field strength [39]. This example demonstrates how time-resolved RIXS can give detailed insight into the properties of short-lived excited states in metal complexes, and how calculations can rationalize the relation between spectra and metal–ligand orbital interactions.

4.4 Multiconfigurational Description of Multiplet Splittings

After showing how X-ray modeling can be used to get insights into molecular orbital interactions, the next level of detail is to look at the different electronic states that arise from a given electron configuration. These states are split by differences in spin and spatial orientation of the electrons, here referred to as multiplet splittings. If these states can be resolved, this gives the most detailed information about the electronic structure of a metal complex. These concepts will be illustrated by first looking at iron K pre-edge XAS, with focus on ferricyanide [33]. This is followed by

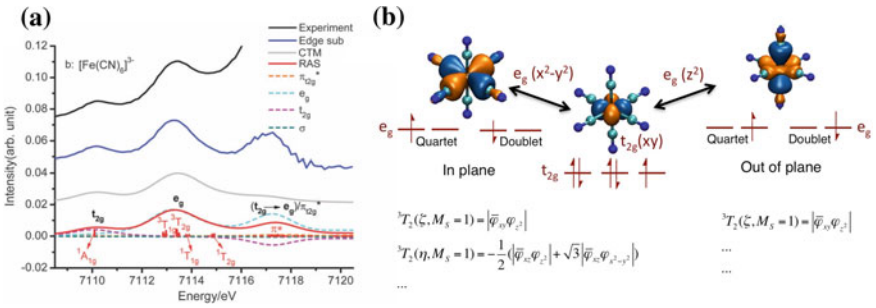

Fig. 14 **a** Iron K pre-edge XAS spectra of ferricyanide. Experimental spectra before and after subtraction of the rising edge are shown in black and blue. Theoretical simulations using CTM and RAS are shown in gray and red. Dashed lines shows the changes in orbital occupation number during the pre-edge process scaled by the intensity of the transition. **b** Orbital interactions in the $t_{2g}^5 e_g^1$ configuration leading to ${}^{1,3}(T_{1g}, T_{2g})$ different states. **c** Selected wavefunctions of the $M_s = 1$ triplet component, without considering spin-orbit coupling. O_h symmetry has been used for labeling of the orbitals. Reproduced from [33] with permission from the Royal Society of Chemistry

an illustration of how the $2p$-$3d$ multiplet interactions in $1s2p$ RIXS directly relates to the strength of σ-bonding in ferrocyanide [32].

Iron K edge XAS corresponds to excitations from the $1s$ orbital. It is commonly used for metal complexes in solution because hard (high-energy) X-rays are only weakly absorbed by the environment. The lowest resonances are typically assigned to $1s \rightarrow 3d$ transitions, see Fig. 1. For centrosymmetric complexes, these transitions are electric dipole forbidden, and for most systems they appear as a weak pre-edge before the rising edge dominated by electric dipole allowed $1s \rightarrow 4p$ transitions. The K pre-edge spectrum of ferricyanide is shown in Fig. 14a. After subtracting the rising edge, three resonances can be identified. These resonances can, as was done for the L-edge XAS spectrum, be labeled t_{2g}, e_g, and a mixed e_g/π^* peak, see Fig. 14a.

The t_{2g} transition results in a closed valence shell, so there is only one final state in this region. The second resonance consists of $1s \rightarrow e_g$ transitions, and the relative position of t_{2g} and e_g resonances reflects the ligand-field strength. A closer analysis shows that resonance is composed of a large number of transitions to different states of the $t_{2g}^5 e_g^1$ configuration, see Fig. 14a. The important $1s$ core hole states are all doublets, like the ground state. However, the relative spin orientations of t_{2g} hole and the e_g electrons can give both singlet and triplet valence states. These are split by differences in exchange interactions. States are further split by the differences in the relative orientation of the e_g electron and the t_{2g} hole. The T_{1g} states represent the energetically more favorable situation where hole and electron are in the same plane, while in the T_{2g} states they are in different planes, see Fig. 14b. A correct description of the properties of these states requires a multiconfigurational approach. It is well known that open-shell singlet states cannot be described by a single determinant. However, some of the wavefunctions of the valence triplet states also require two or more determinants, see Fig. 14c.

The multiplet splittings are directly related to the structure of the molecular orbitals. The t_{2g}-e_g interactions, and thus the multiplet splittings, are largest if both orbitals are localized on the metal, i.e., if they are ionic. The size of the splitting is thus related to the extent of orbital delocalization in the molecule. In practice, the short lifetime of the $1s$ hole gives rise to large lifetime broadenings which can make it difficult to accurately determine the energy of all the states. This limitation can be overcome with the use of RIXS.

4.5 Metal–Ligand Covalency from Multiplet Splittings

RIXS can achieve higher resolution than XAS because the lifetime broadening in the energy transfer direction is determined by the lifetime of the final state after emission. L-edge RIXS can under the right experimental conditions resolve different mutiplet states in the valence region [80], but this requires better resolution than in the study discussed above [53]. Instead, multiplet splittings will be illustrated using $1s2p$ RIXS where the final state has a $2p$ core hole, see Fig. 1 [45, 58]. The same approach has already been used to study how the metal ligands modulate electron transfer in cytochrome c, a key component in cell respiration [44].

$1s2p$ RIXS spectra of ferro- and ferricyanide are shown in Fig. 15 [32, 58, 68]. All spectra have two separate regions, stretching roughly diagonally across the plane. The region at lower energy transfer corresponds to states in the L_3 edge of the XAS spectrum, while the upper region corresponds to the L_2 edge. The calculated RAS spectra do not include the intense transitions in the rising edge, but reproduce the structure of the pre-edge. The incident energy resonances are the same as in K pre-edge XAS. In ferrocyanide, there are two pre-edge resonances, $1s \rightarrow e_g$ and $1s \rightarrow e_g/\pi^*$, with the latter being hidden under the rising edge in the experimental spectrum [33]. Ferricyanide also has a low-energy $1s \rightarrow t_{2g}$ resonance, and a broad e_g peak split by multiplet interactions as shown in Fig. 14a.

It is most instructive to look at the e_g resonance in ferrocyanide. Along the incident energy axis, it does not contain much information because it corresponds to a single state. More information can be obtained from the energy transfer direction. The $2p \rightarrow 1s$ emission from the intermediate state lead to $2p^5 t_{2g}^6 e_g^1$ final states, nominally the same as in L-edge XAS. An L-edge-like spectrum is obtained by taking a vertical cut along constant incident energy (CIE) through the maximum of the e_g resonance, see Fig. 15. With only a single incident energy resonance, it could be expected that the e_g part of the CIE cut and the L-edge XAS should look similar. Instead, the width of the e_g resonance increases from the 0.8 eV in the L-edge spectrum to 1.5 eV in the CIE spectrum, see Fig. 16a. As the experimental broadenings are similar in the two experiments, the explanation is instead the differences in selection rules [58].

The $2p^5 t_{2g}^6 e_g^1$ configuration gives T_{1u} and T_{2u} states. The single-photon electric dipole transitions in XAS only reach T_{1u} states from the $^1A_{1g}$ ground state, while the two-photon RIXS process reaches both T_{1u} and T_{2u} final states, see Fig. 16b.

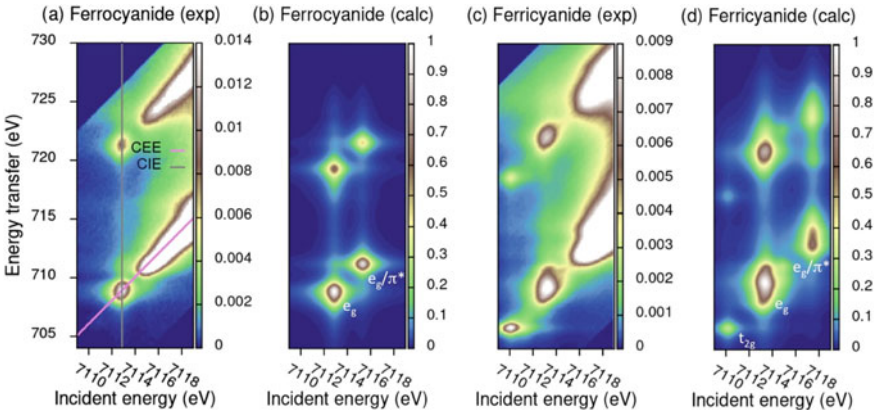

Fig. 15 Experimental and RASPT2 calculated $1s2p$ RIXS planes of iron hexacyanides [32, 58]. Cuts along constant incident energy (CIE) and constant emission energy (CEE) are shown with gray and pink lines, respectively. The RAS spectra only describe pre-edge absorption and the rising edges are not included. Reproduced from [32] with permission from the American Chemical Society

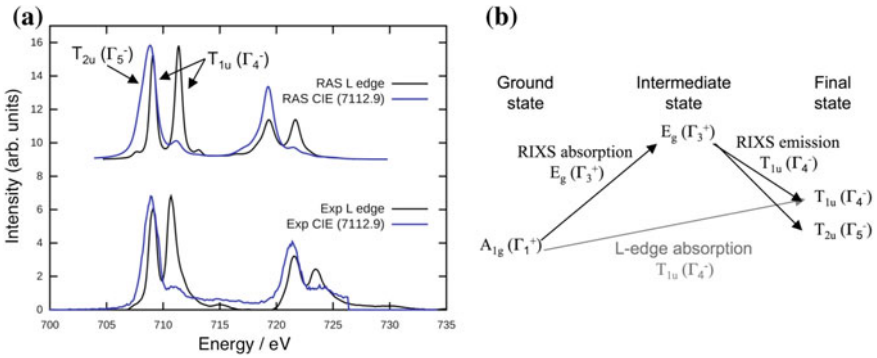

Fig. 16 **a** Iron L-edge XAS and CIE cut through the e_g pre-edge peak for ferrocyanide from RAS modeling (top) and experiment (bottom). **b** Relevant selection rules in O_h symmetry for $1s2p$ RIXS and L-edge XAS from the A_{1g} ground state in low-spin ferrous complexes. Adapted from [32] with permission from the American Chemical Society

This effect is captured in RAS simulations, and the molecular orbital representation can be used to visualize the differences between these states. In analogy to the different $t_{2g}^5 e_g^1$ valence states in Fig. 14, the T_{2u} states are lower in energy because of more favorable in-plane interactions between the $2p$ hole and the e_g electron. As the $2p$ core hole probe is completely localized on the metal, the strength of the interaction measures the amount of metal character in the e_g orbital, with more metal character corresponding to lower metal–ligand covalency. This has been shown experimentally by comparisons between ferrocyanide and ferrous tacn (tacn =1,4,7 triazacyclononane). The latter ligand is a weaker σ donor, leading to less covalent

bonds and more localized 3*d* orbitals, which is seen in a significantly larger width of the e_g resonance of ferrous tacn [58]. Notice that the individual states are actually not resolved in the experiment. It is instead the differences in selection rules that makes it possible to identify the different energy regions for T_{1u} and T_{2u} states.

5 Extensions to Metal Dimers and Complex Systems

All systems previously discussed in this chapter have been relatively small and included no more than one transition metal atom. Many catalytic systems include two or more metal atoms, but multiconfigurational calculations of X-ray processes for such systems are challenging. Including two instead of one metal basically doubles the number of core and valence orbitals and leads to large active spaces. This in turn leads to a very large number of states within the energy range covered by the X-ray spectra [74]. Here two different approaches to RAS modeling of metal dimers are presented. First, a heme dimer with intermolecular coupling between metal atoms is discussed, followed by a μ-oxo bridged metal dimer with covalent coupling [74, 81].

5.1 Intermolecular Coupling

Heme systems play important roles in many biological systems including oxygen transport and catalysis. In many spectral probes, the intense transitions in the porphyrin obscure information about the electronic structure of the iron. This limitation can be overcome with a suitable X-ray probe, and iron L-edge XAS has been successfully used to probe the electronic structure of the Fe–O_2 bond [95]. Another interesting characteristic is that hemes are prone to complexation in solvent. This gives rise to π-π interactions between the porphyrins, as well as resonant coupling of close-lying electronic states of the monomers. These interactions should be detectable in the X-ray signature [74].

RAS simulations have been made of hemin dimers that form in water solvent, see Fig. 17. To avoid treating the full supermolecule, the relevant valence and core-hole states of each monomer are calculated first. The configurations with energies close to X-ray resonances are then extracted. XAS and RIXS correspond to one and two-particle excitations correspondingly, and the full set of states necessary to model these processes can at a first approximation be modeled using a configuration interaction model including singles and doubles (CISD) [74]. After reduction of the size of the interaction matrix by ignoring some contributions, diagonalization gives the states of the full dimer from which X-ray intensities can be calculated.

The simulated spectra of three different dimer orientations are shown as CIE cuts through the L-edge RIXS planes, see Fig. 17. Some resonances show distinct changes, including the elastic peak at 0 eV energy transfer. The magnitude of these

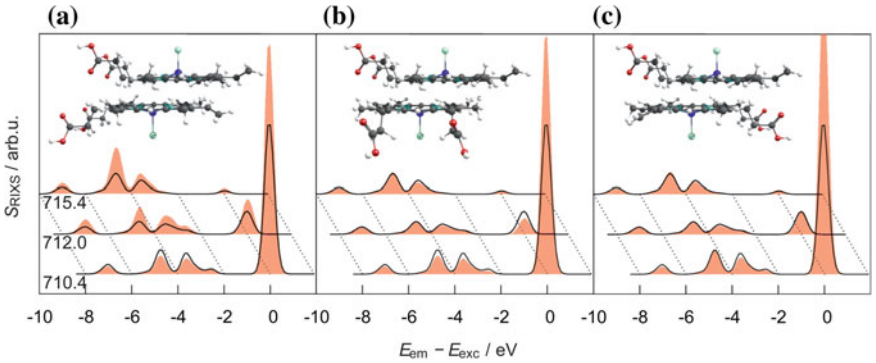

Fig. 17 CIE cuts of the simulated L-edge RIXS spectra of the [Heme B-Cl]^0 dimer (red filled curves) with different orientations of the COOH groups **a** 0, **b** 90, and **c** 180 for three incident energy resonances energies. The monomer spectra are shown as black lines for comparison. Reproduced from [74] and made available under a Creative Commons 4.0 license

changes depends on the molecular orientation, with larger effects in transitions that involve orbitals oriented out of the plane of the porphyrin. These calculations show the sensitivity of the RIXS probe to heme dimerization, but a direct comparison to experiment probably requires more extensive sampling of different orientations [74].

5.2 Intramolecular Coupling

Metal complexes with strong covalent coupling between metals are important in many catalytic systems. For these systems, it is more difficult to separate the active spaces of the two metal centers, which puts severe limitations on the modeling. This is illustrated for the iron K pre-edge spectra of the (hedta)$Fe^{III}$$\mu$–O$Fe^{III}$(hedta) (hedta = N-hydroxyethyl-ethylenediamine-triacetic acid) metal dimer, see Fig. 18a [81]. The K pre-edge is sensitive to both geometric and electronic structure [94]. In iron dimers, deviations from centrosymmetry caused by the metal–metal interactions lead to electric dipole contributions in addition to what is usually referred to as electric quadrupole transitions.

The RAS spectrum was calculated with 13 valence orbitals in the active space, three Fe(3d)–O(p) bonding orbitals, seven metal-3*d*-dominated orbitals and three antibonding iron–oxygen orbitals, see Fig. 18b. The ground state has antiferromagnetic coupling between two high-spin $3d^5$ centers, giving an open-shell singlet. However, due to the challenges to calculate the very large number of singlet states, simulations were instead made using the ferromagnetically coupled undectet, which lies 0.1 eV above the ground state. This leads to a significant reduction in the number of possible states and enables the calculation of the full K pre-edge spectrum.

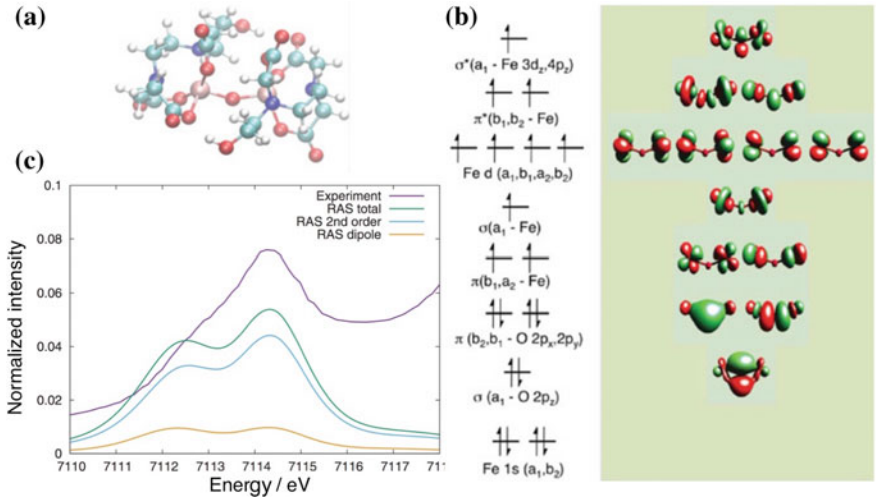

Fig. 18 **a** Structure of [(hedta)FeOFe(hedta)]. RAS active space for Fe_2O. Experimental and RASSCF/ANO-RCC-VTZP simulated K pre-edge spectra of [(hedta)FeOFe(hedta)] [81, 94]. Adapted from [81] with permission from Taylor and Francis

The experimental K pre-edge of the hedta dimer has two discernible features with an energy splitting around 1.7 eV, see Fig. 18 [94]. The RASSCF spectrum also shows two distinct pre-edge features, with a more intense peak at higher energy. According to the simulations, there are non-negligible contributions from electric dipole contributions, but the largest intensity still comes from quadrupole contributions. The energy splitting is overestimated by 0.4 eV and the low-energy peak appears more intense in the simulated spectrum. These deviations could possibly decrease with use of PT2 corrections, but this was not tested due to the high-computational cost. The challenges in modeling X-ray spectra of covalently linked metal clusters illustrate the need for further development of the multiconfigurational approach.

6 Conclusions and Outlook

By its position at the intersection of theory and experiment, the field of ab initio X-ray simulations combines the strengths of both. Theory provides insight into the chemical process while the experiment can be used to verify the theoretical findings. This is particularly relevant for transition metal catalysts, where accurate theoretical predictions are often difficult. In recent years, multiconfigurational calculations have become a reference for accurate X-ray simulations for transition metal complexes. Thanks to the inherent flexibility of the method, and helped by constant developments, most X-ray spectroscopies can now be simulated and many interesting applications have already been performed, showcasing the strong promises of this field.

Yet, the X-ray modeling field is still evolving rapidly. This is certainly true for the multiconfigurational approach, with new method developments constantly shaping the way these calculations are performed. This process is likely to continue and already now, many developments in related fields offer great promises to lift some of the main limitations of the method. As an example, the CPP approach has been applied to many wavefunction models to efficiently compute the spectrum at any energy range [22]. While not available yet, an efficient CPP-CAS/RAS implementation would alleviate the cost associated with the high density of states. It could also provide higher accuracy by, for example, allowing core relaxation and ensuring better consistency between different calculations by removing artifacts caused by state averaging.

Similarly, while multiconfigurational simulations have mainly been limited to a single metal atom because of active-space restrictions, many techniques have been developed recently to push this limit, e.g., the density matrix renormalization group [15], full CI quantum Monte Carlo [12], or Heat-Bath CI [37]. While those methods still have not been used to compute X-ray spectra, and some technical difficulties are still left to be overcome, the potential to calculate X-ray spectra of some of the fascinating natural and synthetic multi-metallic complexes at the multiconfigurational level is certainly very appealing. Those developments, and others yet unforeseen, will shape the future of the field and push the limits of what can be done, hopefully matching the significant advances in the experimental techniques. This can only improve the already strong complementarity between theory and experiment and deepen our insights into the captivating world of transition metal catalysis.

Acknowledgements We acknowledge financial support from the foundation Olle Engkvist Byggmastare and the Knut and Alice Wallenberg Foundation (Grant No. KAW-2013.0020). We thank Meiyuan Guo and Michael Odelius for useful discussions.

References

1. Ågren H, Jensen HJA (1987) An efficient method for the calculation of generalized overlap amplitudes for core photoelectron shake-up spectra. Chem Phys Lett 137(5):431–436
2. Ågren H, Flores-Riveros A, Jensen HJA (1989) An efficient method for calculating molecular radiative intensities in the vuv and soft x-ray wavelength regions. Phys Scr 40(6):745
3. Andersson K, Malmqvist PÅ, Roos BO, Sadlej AJ, Wolinski K (1990) Second-order perturbation theory with a casscf reference function. J Phys Chem 94(14):5483–5488
4. Angeli C, Cimiraglia R, Evangelisti S, Leininger T, Malrieu JP (2001) Introduction of n-electron valence states for multireference perturbation theory. J Chem Phys 114(23):10252–10264. https://doi.org/10.1063/1.1361246
5. Aquilante F, Autschbach J, Carlson RK, Chibotaru LF, Delcey MG, De Vico L, Fdez Galván I, Ferre N, Frutos LM, Gagliardi L et al (2016) Molcas 8: new capabilities for multiconfigurational quantum chemical calculations across the periodic table. J Comput Chem 37(5):506–541
6. Atak K, Bokarev SI, Gotz M, Golnak R, Lange KM, Engel N, Dantz M, Suljoti E, Kühn O, Aziz EF (2013) Nature of the chemical bond of aqueous Fe2+ probed by soft X-ray spectroscopies and ab initio calculations. J Phys Chem B 117(41):12613–12618

7. Bagus PS, Nelin CJ, Ilton ES, Sassi MJ, Rosso KM (2017) Analysis of X-ray adsorption edges: L2,3 edge of $FeCl_4^-$. J Chem Phys 147(22):224306. https://doi.org/10.1063/1.5006223
8. Bernadotte S, Atkins AJ, Jacob CR (2012) Origin-independent calculation of quadrupole intensities in X-ray spectroscopy. J Chem Phys 137(20):204106
9. Blomberg MR, Siegbahn PE (1997) A comparative study of high-spin manganese and iron complexes. Theor Chem Acc 97(1–4):72–80
10. Bokarev SI, Dantz M, Suljoti E, Kühn O, Aziz EF (2013) State-dependent electron delocalization dynamics at the solute-solvent interface: soft-x-ray absorption spectroscopy and ab initio calculations. Phys Rev Lett 111(8):083002–083007
11. Bokarev SI, Khan M, Abdel-Latif MK, Xiao J, Hilal R, Aziz SG, Aziz EF, Kühn O (2015) Unraveling the electronic structure of photocatalytic manganese complexes by L-edge X-ray spectroscopy. J Phys Chem C 119(33):19192–19200
12. Booth GH, Thom AJW, Alavi A (2009) Fermion monte carlo without fixed nodes: a game of life, death, and annihilation in slater determinant space. J Chem Phys 131(5):054106. https://doi.org/10.1063/1.3193710
13. Bunău O, Joly Y (2012) Full potential x-ray absorption calculations using time dependent density functional theory. J Phys: Condens Matter 24(21):215502. http://stacks.iop.org/0953-8984/24/i=21/a=215502
14. Cederbaum LS, Domcke W, Schirmer J (1980) Many-body theory of core holes. Phys Rev A 22:206–222. https://doi.org/10.1103/PhysRevA.22.206
15. Chan GKL, Sharma S (2011) The density matrix renormalization group in quantum chemistry. Annu Rev Phys Chem 62(1):465–481. https://doi.org/10.1146/annurev-physchem-032210-103338 (pMID: 21219144)
16. Chantzis A, Kowalska JK, Maganas D, DeBeer S, Neese F (2018) Ab initio wave function-based determination of element specific shifts for the efficient calculation of x-ray absorption spectra of main group elements and first row transition metals. J Chem Theory Comput 14(7):3686–3702. https://doi.org/10.1021/acs.jctc.8b00249 (pMID: 29894196)
17. Coriani S, Christiansen O, Fransson T, Norman P (2012) Coupled-cluster response theory for near-edge x-ray-absorption fine structure of atoms and molecules. Phys Rev A 85:022507. https://link.aps.org/doi/10.1103/PhysRevA.85.022507
18. Cossi M, Barone V (2000) Solvent effect on vertical electronic transitions by the polarizable continuum model. J Chem Phys 112(5):2427–2435
19. Cramer S, DeGroot F, Ma Y, Chen C, Sette F, Kipke C, Eichhorn D, Chan M, Armstrong W (1991) Ligand field strengths and oxidation states from manganese L-edge spectroscopy. J Am Chem Soc 113(21):7937–7940
20. De Groot F (2001) High-resolution x-ray emission and x-ray absorption spectroscopy. Chem Rev 101(6):1779–1808
21. Douglas M, Kroll NM (1974) Quantum electrodynamical corrections to the fine structure of helium. Ann Phys 82(1):89–155
22. Ekström U, Norman P, Carravetta V, Ågren H (2006) Polarization propagator for x-ray spectra. Phys Rev Lett 97:143001. http://link.aps.org/doi/10.1103/PhysRevLett.97.143001
23. Engel N, Bokarev SI, Suljoti E, Garcia-Diez R, Lange KM, Atak K, Golnak R, Kothe A, Dantz M, Kühn O, Aziz EF (2014) Chemical bonding in aqueous ferrocyanide: experimental and theoretical X-ray spectroscopic study. J Phys Chem B 118(6):1555–1563
24. Forsberg N, Malmqvist PÅ (1997) Multiconfiguration perturbation theory with imaginary level shift. Chem Phys Lett 274(1):196–204
25. Gel'mukhanov F, Ågren H (1999) Resonant x-ray raman scattering. Phys Rep 312(3–6):87–330
26. Ghigo G, Roos BO, Malmqvist PÅ (2004) A modified definition of the zeroth-order Hamiltonian in multiconfigurational perturbation theory (CASPT2). Chem Phys Lett 396(1):142–149
27. Golnak R, Bokarev SI, Seidel R, Xiao J, Grell G, Atak K, Unger I, Thürmer S, Aziz SG, Kühn O et al (2016a) Joint analysis of radiative and non-radiative electronic relaxation upon X-ray irradiation of transition metal aqueous solutions. Sci Rep 6:24659
28. Golnak R, Xiao J, Atak K, Unger I, Seidel R, Winter B, Aziz EF (2016b) Undistorted X-ray absorption spectroscopy using s-core-orbital emissions. J Phys Chem A 120(18):2808–2814

29. Grell G, Bokarev SI, Winter B, Seidel R, Aziz EF, Aziz SG, Kühn O (2015) Multi-reference approach to the calculation of photoelectron spectra including spin-orbit coupling. J Chem Phys 143(7):074104
30. Grell G, Bokarev SI, Winter B, Seidel R, Aziz EF, Aziz SG, Kühn O (2016) Erratum: multi-reference approach to the calculation of photoelectron spectra including spin-orbit coupling. J Chem Phys 143:074104 (2015). J Chem Phys 145(8):089901
31. de Groot F (2005) Multiplet effects in X-ray spectroscopy. Coord Chem Rev 249(1):31–63
32. Guo M, Källman E, Sørensen LK, Delcey MG, Pinjari RV, Lundberg M (2016a) Molecular orbital simulations of metal 1s2p resonant inelastic X-ray scattering. J Phys Chem A 120(29):5848–5855
33. Guo M, Sørensen LK, Delcey MG, Pinjari RV, Lundberg M (2016b) Simulations of iron K pre-edge X-ray absorption spectra using the restricted active space method. Phys Chem Chem Phys 18(4):3250–3259
34. Guo M, Källman E, Pinjari RV, Couto RC, Sørensen LK, Lindh R, Pierloot K, Lundberg M (2019) Fingerprinting electronic structure of heme iron by ab initio modeling of metal L-edge X-ray absorption spectra. J Chem Theory Comput 15(1):477–489. https://doi.org/10.1021/acs.jctc.8b00658
35. Hess BA (1986) Relativistic electronic-structure calculations employing a two-component no-pair formalism with external-field projection operators. Phys Rev A 33(6):3742
36. Hocking RK, Wasinger EC, de Groot FM, Hodgson KO, Hedman B, Solomon EI (2006) Fe L-edge XAS studies of $K_4[Fe(CN)_6]$ and K3[$Fe(CN)_6$]: a direct probe of back-bonding. J Am Chem Soc 128(32):10442–10451
37. Holmes AA, Tubman NM, Umrigar CJ (2016) Heat-bath configuration interaction: an efficient selected configuration interaction algorithm inspired by heat-bath sampling. J Chem Theory Comput 12(8):3674–3680. https://doi.org/10.1021/acs.jctc.6b00407 (pMID: 27428771)
38. Jan W, Michael W, Andreas D (2014) Calculating core-level excitations and x-ray absorption spectra of medium-sized closed-shell molecules with the algebraic-diagrammatic construction scheme for the polarization propagator. J Comput Chem 35(26):1900–1915. https://doi.org/10.1002/jcc.23703, https://onlinelibrary.wiley.com/doi/abs/10.1002/jcc.23703
39. Jay RM, Norell J, Eckert S, Hantschmann M, Beye M, Kennedy B, Quevedo W, Schlotter WF, Dakovski GL, Minitti MP, Hoffmann MC, Mitra A, Moeller SP, Nordlund D, Zhang W, Liang HW, Kunnus K, Kubiek K, Techert SA, Lundberg M, Wernet P, Gaffney K, Odelius M, Föhlisch A (2018) Disentangling transient charge density and metalligand covalency in photoexcited ferricyanide with femtosecond resonant inelastic soft X-ray scattering. J Phys Chem Lett 9(12):3538–3543. https://doi.org/10.1021/acs.jpclett.8b01429 (pMID: 29888918)
40. Jensen HJA, Jørgensen P, Ågren H (1987) Efficient optimization of large scale MCSCF wave functions with a restricted step algorithm. J Chem Phys 87(1):451–466
41. Johansson MP, Blomberg MR, Sundholm D, Wikström M (2002) Change in electron and spin density upon electron transfer to haem. Biochim Biophys Acta-Bioenerg 1553(3):183–187
42. Josefsson I, Kunnus K, Schreck S, Föhlisch A, de Groot F, Wernet P, Odelius M (2012) Ab initio calculations of X-ray spectra: atomic multiplet and molecular orbital effects in a multiconfigurational SCF approach to the L-Edge spectra of transition metal complexes. J Phys Chem Lett 3(23):3565–3570. https://doi.org/10.1021/jz301479j
43. Klooster R, Broer R, Filatov M (2012) Calculation of x-ray photoelectron spectra with the use of the normalized elimination of the small component method. Chem Phys 395:122–127
44. Kroll T, Hadt RG, Wilson SA, Lundberg M, Yan JJ, Weng TC, Sokaras D, Alonso-Mori R, Casa D, Upton MH, Hedman B, Hodgson KO, Solomon EI (2014) Resonant inelastic X-ray scattering on ferrous and ferric bis-imidazole porphyrin and cytochrome c: nature and role of the axial methionine-Fe bond. J Am Chem Soc 136(52):18087–18099
45. Kroll T, Lundberg M, Solomon EI (2016) X-ray absorption and RIXS on coordination complexes. In: Van Bokhoven JA, Lamberti C (eds) X-ray absorption and X-ray emission spectroscopy: theory and applications. Wiley, Chichester, pp 407–435
46. Kubin M, Kern J, Gul S, Kroll T, Chatterjee R, Lchel H, Fuller FD, Sierra RG, Quevedo W, Weniger C, Rehanek J, Firsov A, Laksmono H, Weninger C, Alonso-Mori R, Nordlund DL,

Lassalle-Kaiser B, Glownia JM, Krzywinski J, Moeller S, Turner JJ, Minitti MP, Dakovski GL, Koroidov S, Kawde A, Kanady JS, Tsui EY, Suseno S, Han Z, Hill E, Taguchi T, Borovik AS, Agapie T, Messinger J, Erko A, Föhlisch A, Bergmann U, Mitzner R, Yachandra VK, Yano J, Wernet P (2017) Soft x-ray absorption spectroscopy of metalloproteins and high-valent metal-complexes at room temperature using free-electron lasers. Struct Dyn 4(5):054307. https://doi.org/10.1063/1.4986627

47. Kubin M, Guo M, Ekimova M, Baker ML, Kroll T, Källman E, Kern J, Yachandra VK, Yano J, Nibbering ET, Lundberg M, Wernet P (2018) Direct determination of absolute absorption cross sections at the L-Edge of dilute Mn complexes in solution using a transmission flatjet. Inorg Chem 57(9):5449–5462
48. Kubin M, Guo M, Ekimova M, Källman EJ, Kern J, Yachandra VK, Yano J, Nibbering ET, Lundberg M, Wernet P (2018) Cr L-edge X-ray absorption spectroscopy of CrIII $(acac)_3$ in solution with measured and calculated absolute absorption cross sections. J Phys Chem B. https://doi.org/10.1021/acs.jpcb.8b04190
49. Kubin M, Guo M, Kroll T, Löchel H, Källman E, Baker ML, Mitzner R, Gul S, Kern J, Föhlisch A, Erko A, Bergmann U, Yachandra VK, Yano J, Lundberg M, Wernet P (2018) Probing the oxidation state of transition metal complexes: a case study on how charge and spin densities determine Mn L-Edge X-ray absorption energies. Chem Sci. https://doi.org/10.1039/C8SC00550H
50. Kubin M, Kern J, Guo M, Källman E, Mitzner R, Yachandra VK, Lundberg M, Yano J, Wernet P (2018) X-ray-induced sample damage at the Mn L-edge: a case study for soft X-ray spectroscopy of transition metal complexes in solution. Phys Chem Chem Phys 20:16817–16827
51. Kunnus K, Josefsson I, Rajkovic I, Schreck S, Quevedo W, Beye M, Grbel S, Scholz M, Nordlund D, Zhang W, Hartsock RW, Gaffney KJ, Schlotter WF, Turner JJ, Kennedy B, Hennies F, Techert S, Wernet P, Odelius M, Fhlisch A (2016) Anti-stokes resonant x-ray Raman scattering for atom specific and excited state selective dynamics. New J Phys 18(10):103011. http://stacks.iop.org/1367-2630/18/i=10/a=103011
52. Kunnus K, Josefsson I, Rajkovic I, Schreck S, Quevedo W, Beye M, Weniger C, Grbel S, Scholz M, Nordlund D, Zhang W, Hartsock RW, Gaffney KJ, Schlotter WF, Turner JJ, Kennedy B, Hennies F, de Groot FMF, Techert S, Odelius M, Wernet P, Fhlisch A (2016) Identification of the dominant photochemical pathways and mechanistic insights to the ultrafast ligand exchange of $Fe(CO)_5$ to $Fe(CO)_4EtOH$. Struct Dyn 3(4):043204. https://doi.org/10.1063/1.4941602
53. Kunnus K, Zhang W, Delcey MG, Pinjari RV, Miedema PS, Schreck S, Quevedo W, Schroeder H, Föhlisch A, Gaffney KJ, Lundberg M, Odelius M, Wernet P (2016) Viewing the valence electronic structure of ferric and ferrous hexacyanide in solution from the Fe and cyanide perspectives. J Phys Chem B 120(29):7182–7194. https://doi.org/10.1021/acs.jpcb.6b04751
54. Liang W, Fischer SA, Frisch MJ, Li X (2011) Energy-specific linear response TDHF/TDDFT for calculating high-energy excited states. J Chem Theory Comput 7(11):3540–3547. https://doi.org/10.1021/ct200485x
55. List NH, Kauczor J, Saue T, Jensen HJA, Norman P (2015) Beyond the electric-dipole approximation: a formulation and implementation of molecular response theory for the description of absorption of electromagnetic field radiation. J Chem Phys 142(24):244111
56. List NH, Saue T, Norman P (2017) Rotationally averaged linear absorption spectra beyond the electric-dipole approximation. Mol Phys 115(1–2):63–74
57. Liu Y, Persson P, Sundström V, Wärnmark K (2016) Fe N-heterocyclic carbene complexes as promising photosensitizers. Acc Chem Res 49(8):1477–1485
58. Lundberg M, Kroll T, DeBeer S, Bergmann U, Wilson SA, Glatzel P, Nordlund D, Hedman B, Hodgson KO, Solomon EI (2013) Metal-ligand covalency of iron complexes from high-resolution resonant inelastic X-ray scattering. J Am Chem Soc 135(45):17121–17134. https://doi.org/10.1021/ja408072q (pMID: 24131028)
59. Ma D, Li Manni G, Gagliardi L (2011) The generalized active space concept in multiconfigurational self-consistent field methods. J Chem Phys 135(4):044128. https://doi.org/10.1063/1.3611401

60. Maganas D, DeBeer S, Neese F (2014) Restricted open-shell configuration interaction cluster calculations of the L-Edge X-ray absorption study of TiO_2 and CaF_2 solids. Inorg Chem 53(13):6374–6385. https://doi.org/10.1021/ic500197v (pMID: 24871209)
61. Malmqvist PÅ (1986) Calculation of transition density matrices by nonunitary orbital transformations. Int J Quantum Chem 30(4):479–494. https://doi.org/10.1002/qua.560300404
62. Malmqvist PÅ, Rendell A, Roos BO (1990) The restricted active space self-consistent-field method, implemented with a split graph unitary group approach. J Phys Chem 94(14):5477–5482. https://doi.org/10.1021/j100377a011
63. Malmqvist PÅ, Roos BO, Schimmelpfennig B (2002) The restricted active space (RAS) state interaction approach with spin-orbit coupling. Chem Phys Lett 357(3):230–240
64. Malmqvist PÅ, Pierloot K, Shahi ARM, Cramer CJ, Gagliardi L (2008) The restricted active space followed by second-order perturbation theory method: theory and application to the study of CuO_2 and Cu_2O_2 systems. J Chem Phys 128(20):204109
65. Nakata A, Imamura Y, Otsuka T, Nakai H (2006) Time-dependent density functional theory calculations for core-excited states: assessment of standard exchange-correlation functionals and development of a novel hybrid functional. J Chem Phys 124(9):094105. https://doi.org/10.1063/1.2173987
66. Norell J, Jay RM, Hantschmann M, Eckert S, Guo M, Gaffney KJ, Wernet P, Lundberg M, Föhlisch A, Odelius M (2018) Fingerprints of electronic, spin and structural dynamics from resonant inelastic soft X-ray scattering in transient photo-chemical species. Phys Chem Chem Phys 20(10):7243–7253
67. Norman P, Dreuw A (2018) Simulating X-ray spectroscopies and calculating core-excited states of molecules. Chem Rev 118(15):7208–7248
68. Penfold TJ, Reinhard M, Rittmann-Frank MH, Tavernelli I, Rothlisberger U, Milne CJ, Glatzel P, Chergui M (2014) X-ray spectroscopic study of solvent effects on the ferrous and ferric hexacyanide anions. J Phys Chem A 118(40):9411–9418
69. Pierloot K (2003) The CASPT2 method in inorganic electronic spectroscopy: from ionic transition metal to covalent actinide complexes. Mol Phys 101(13):2083–2094
70. Pierloot K, Phung QM, Domingo A (2017) Spin state energetics in first-row transition metal complexes: contribution of (3s3p) correlation and its description by second-order perturbation theory. J Chem Theory Comput 13(2):537–553. https://doi.org/10.1021/acs.jctc.6b01005 (pMID: 28005368)
71. Pinjari RV, Delcey MG, Guo M, Odelius M, Lundberg M (2014) Restricted active space calculations of L-edge X-ray absorption spectra: From molecular orbitals to multiplet states. J Chem Phys 141(12):124116
72. Pinjari RV, Delcey MG, Guo M, Odelius M, Lundberg M (2015) Erratum: restricted active space calculations of L-edge X-ray absorption spectra: from molecular orbitals to multiplet states. J Chem Phys 141:124116 (2014)]. J Chem Phys 142(6):069901
73. Pinjari RV, Delcey MG, Guo M, Odelius M, Lundberg M (2016) Cost and sensitivity of restricted active-space calculations of metal L-edge X-ray absorption spectra. J Comput Chem 37(5):477–486
74. Preuße M, Bokarev SI, Aziz SG, Kühn O (2016) Towards an ab initio theory for metal L-edge soft X-ray spectroscopy of molecular aggregates. Struct Dynam 3(6):062601
75. Roemelt M, Maganas D, DeBeer S, Neese F (2013) A combined DFT and restricted open-shell configuration interaction method including spin-orbit coupling: application to transition metal L-edge X-ray absorption spectroscopy. J Chem Phys 138(20):204101
76. Roos BO (1980) The complete active space SCF method in a fock-matrix-based super-CI formulation. Int J Quantum Chem 18(S14):175–189. https://doi.org/10.1002/qua.560180822
77. Roos BO, Lindh R, Malmqvist PÅ, Veryazov V, Widmark PO (2004) Main group atoms and dimers studied with a new relativistic ANO basis set. J Phys Chem A 108(15):2851–2858
78. Roos BO, Lindh R, Malmqvist PÅ, Veryazov V, Widmark PO (2005) New relativistic ANO basis sets for transition metal atoms. J Phys Chem A 109(29):6575–6579
79. Roos BO, Lindh R, Malmqvist PÅ, Veryazov V, Widmark PO (2016) Multiconfigurational quantum chemistry. Wiley, New York

80. van Schooneveld MM, Juhin A, Campos-Cuerva C, Schmitt T, de Groot FM (2013) Origin of low energy d-d excitations observed on wet chemically prepared cobalt bearing nanoparticles by 2p3d resonant X-ray emission spectroscopy. J Phys Chem C 117(27):14398–14407
81. Sørensen LK, Guo M, Lindh R, Lundberg M (2017) Applications to metal K pre-edges of transition metal dimers illustrate the approximate origin independence for the intensities in the length representation. Mol Phys 115(1–2):174–189
82. Sørensen LK, Kieri E, Srivastava S, Lundberg M, Lindh R (2019) Implementation of the exact semiclassical light-matter interaction using the Gauss-Hermite quadrature: A simple alternative to the multipole expansion. Phys Rev A 99(013419):1–11. https://doi.org/10.1103/PhysRevA.99.013419
83. Stein CJ, Reiher M (2016) Automated selection of active orbital spaces. J Chem Theory Comput 12(4):1760–1771. https://doi.org/10.1021/acs.jctc.6b00156 (pMID: 26959891)
84. Stener M, Fronzoni G, de Simone M (2003) Time dependent density functional theory of core electrons excitations. Chem Phys Lett 373(1):115–123. https://doi.org/10.1016/S0009-2614(03)00543-8
85. Stenrup M, Lindh R, Fdez Galván I (2015) Constrained numerical gradients and composite gradients: practical tools for geometry optimization and potential energy surface navigation. J Comput Chem 36(22):1698–1708
86. Suljoti E, Garcia-Diez R, Bokarev SI, Lange KM, Schoch R, Dierker B, Dantz M, Yamamoto K, Engel N, Atak K, Kuhn O, Bauer M, Rubensson JE, Aziz EF (2013) Direct observation of molecular orbital mixing in a solvated organometallic complex. Angew Chem Int Ed 52(37):9841–9844. https://doi.org/10.1002/anie.201303310, https://onlinelibrary.wiley.com/doi/abs/10.1002/anie.201303310
87. Tanaka A, Jo T (1994) Resonant 3d, 3p and 3s photoemission in transition metal oxides predicted at 2p threshold. J Phys Soc JPN 63(7):2788–2807
88. Thürmer S, Seidel R, Eberhardt W, Bradforth SE, Winter B (2011) Ultrafast hybridization screening in Fe3+ aqueous solution. J Am Chem Soc 133(32):12528–12535
89. Van Schooneveld M, DeBeer S (2015) A close look at dose: toward l-edge xas spectral uniformity, dose quantification and prediction of metal ion photoreduction. J Electron Spectrosc Relat Phenom 198:31–56
90. Wang H, Bokarev SI, Aziz SG, Kühn O (2017) Ultrafast spin-state dynamics in transition-metal complexes triggered by soft-X-ray light. Phys Rev Lett 118(2):023001
91. Wasinger EC, De Groot FM, Hedman B, Hodgson KO, Solomon EI (2003) L-edge X-ray absorption spectroscopy of non-heme iron sites: experimental determination of differential orbital covalency. J Am Chem Soc 125(42):12894–12906
92. Wernet P, Kunnus K, Schreck S, Quevedo W, Kurian R, Techert S, de Groot FM, Odelius M, Föhlisch A (2012) Dissecting local atomic and intermolecular interactions of transition-metal ions in solution with selective X-ray spectroscopy. J Phys Chem Lett 3(23):3448–3453
93. Wernet P, Kunnus K, Josefsson I, Rajkovic I, Quevedo W, Beye M, Schreck S, Gruebel S, Scholz M, Nordlund D, Zhang W, Hartsock RW, Schlotter WF, Turner JJ, Kennedy B, Hennies F, de Groot FMF, Gaffney KJ, Techert S, Odelius M, Foehlisch A (2015) Orbital-specific mapping of the ligand exchange dynamics of $Fe(CO)_5$ in solution. Nature 520(7545):78–81
94. Westre TE, Kennepohl P, DeWitt JG, Hedman B, Hodgson KO, Solomon EI (1997) A multiplet analysis of Fe K-edge 1s 3d pre-edge features of iron complexes. J Am Chem Soc 119(27):6297–6314
95. Wilson SA, Kroll T, Decreau RA, Hocking RK, Lundberg M, Hedman B, Hodgson KO, Solomon EI (2013) Iron L-Edge X-ray absorption spectroscopy of oxy-picket fence porphyrin: experimental insight into Fe-O_2 bonding. J Am Chem Soc 135(3):1124–1136
96. Yano J, Yachandra V (2014) Mn_4Ca cluster in photosynthesis: where and how water is oxidized to dioxygen. Chem Rev 114(8):4175–4205
97. Zobel JP, Nogueira JJ, Gonzalez L (2017) The ipea dilemma in caspt2. Chem Sci 8:1482–1499. https://doi.org/10.1039/C6SC03759C